Research Square

Preprints are preliminary reports that have not undergone peer review.
They should not be considered conclusive, used to inform clinical practice,
or referenced by the media as validated information.

Joint attenuation of random and erratic seismic noise via automated dataset construction and model hyper-parameters tuning workflow

Mingde Chen
Cooperative Innovation Center of Unconventional Oil and Gas (Ministry of Education and Hubei Province), Yangtze University

Rui Guo
BGP Inc., China National Petroleum Corporation

Aohuai Pan
Changsha Uranium Geology Research Institute, China National Nuclear Corporation

Chen Li
Cooperative Innovation Center of Unconventional Oil and Gas (Ministry of Education and Hubei Province), Yangtze University

Wei Chen
Cooperative Innovation Center of Unconventional Oil and Gas (Ministry of Education and Hubei Province), Yangtze University

Zhixian Gui
gyy68@126.com

Cooperative Innovation Center of Unconventional Oil and Gas (Ministry of Education and Hubei Province), Yangtze University

Article

Keywords:

Posted Date: November 24th, 2026

DOI: https://doi.org/10.21203/rs.3.rs-11550033/v1

License: This work is licensed under a Creative Commons Attribution 4.0 International License.
Read Full License

Additional Declarations: No competing interests reported.

Joint attenuation of random and erratic seismic noise via automated dataset construction and model hyper-parameters tuning workflow

Mingde Chen[1], Rui Guo[2], Aohuai Pan[3], Chen Li[1], Wei Chen[1], Zhixian Gui[1*]

[1]Cooperative Innovation Center of Unconventional Oil and Gas (Ministry of Education and Hubei Province), Yangtze University, Wuhan, 430100, China.

[2]BGP Inc., China National Petroleum Corporation, Zhuozhou, 072751, China.

[3]Changsha Uranium Geology Research Institute, China National Nuclear Corporation, Changsha, China.

*Corresponding author(s). E-mail(s): gyy68@126.com;
Contributing authors: chenmingde1999@163.com;
guorui198428@163.com; 915232363@qq.com; 823237762@qq.com;
chenwei2014@yangtzeu.edu.cn;

Abstract

Seismic data contain information about the physical properties and spatial distribution of subsurface media, yet noise attenuation remains a longstanding challenge in seismic processing. In particular, the incoherent nature of erratic and random noise makes it difficult to recover the underlying signal from noisy records. Deep learning offers a data-driven alternative, but existing workflows generally require laborious training-data preparation and hyper-parameter tuning, and may generalize poorly to field data acquired in geologically complex and variable settings. We therefore propose a fully automated workflow for seismic denoising. It constructs structurally diverse training data by selecting a representative section from each of multiple three-dimensional synthetic seismic volumes, sequentially screens network hyper-parameters within expert-constrained search spaces using signal-to-noise ratio as the primary metric. The workflow combines adaptive Huber and structural similarity losses to reduce sensitivity to erratic noise while preserving seismic structures; the loss-balance factor is tuned

automatically and the Huber threshold is estimated adaptively for each batch. Experiments on synthetic data and field land and marine seismic data, conducted under an open-source and reproducible protocol, show that the workflow outperforms the selected conventional and deep-learning baselines in noise attenuation and effective-signal preservation. The results demonstrate the significant potential of automated, traceable workflows for intelligent seismic data processing. Code and data are available at https //github.com/fathercharose/automated-seismic-denoising-workflow.

Keywords: deep learning, automated workflow, seismic denoising, hyper-parameter tuning

1 Introduction

Seismic exploration records and analyzes seismic wave responses in the subsurface to provide information about the physical properties, spatial distribution, and structural geometry of underground media. Rather than observing subsurface structures directly, it infers subsurface information from a limited set of surface or borehole recordings. Data quality therefore directly affects subsequent seismic imaging, structural interpretation, attribute analysis, and inversion. The objective of seismic data processing extends beyond improving visual clarity: it seeks to attenuate unwanted energy mixed with the useful signal while preserving reflection events, amplitude variations, and structural boundaries as faithfully as possible. As exploration increasingly targets areas with more complex structures, weaker signals, and less stable acquisition conditions, reliable recovery of useful seismic information from noisy observations has become a fundamental challenge in seismic data processing [1, 2].

Noise in field seismic records has diverse origins, including environmental disturbances, instrument responses, changes in acquisition conditions, and human activities. In terms of spatial correlation and observed characteristics, two types of incoherent noise warrant particular distinction. Random noise typically lacks stable spatial patterns and waveform characteristics, and its frequency content can overlap substantially with that of useful reflections. Erratic noise, by contrast, often appears as localized, isolated, high-amplitude anomalies with pronounced non-Gaussian characteristics [3, 4]. These components may coexist in field data, so noise cannot always be treated as a small, uniformly distributed perturbation. Random noise reduces reflection continuity and signal-to-noise ratio (SNR), whereas erratic noise can distort local amplitude relationships, obscure weak reflections, and hinder the identification of structural boundaries. Insufficient attenuation allows residual noise to propagate into imaging, interpretation, and inversion; excessive processing can remove useful signal that overlaps noise in frequency or spatial location. Joint attenuation of random and erratic noise is therefore a recovery problem that must account for statistical outliers, structural continuity, and signal fidelity simultaneously. Previous work has formulated it as the joint recovery of a structured signal and sparse anomalous components [5],

but conventional workflows can still leave residual noise and cause signal leakage under strong erratic interference [6].

Conventional seismic noise attenuation methods follow several established approaches. The first exploits the local temporal or spatial predictability of useful seismic signals, estimating and suppressing noise through predictive filtering or autoregressive modeling [7]. These methods are effective when signals exhibit strong local regularity, but their predictive models can become inaccurate where reflection geometry changes rapidly, events are discontinuous near faults, or noise and useful signals occupy similar frequency bands. The second approach exploits sparsity or signal–noise separability in a transform domain, using wavelet, curvelet, and Seislet transforms or sparse representations to separate noise from signal [8, 9]. Its effectiveness depends on the choice of transform basis, decomposition scales, and thresholds. Where noise and useful events overlap in the transform domain, a threshold that is too low leaves residual noise, whereas an excessive threshold removes signal details. The third approach organizes seismic data into Hankel, Toeplitz, or other structured matrices and performs rank reduction by exploiting the low-rank properties of the useful signal [10, 11]. Low-rank methods exploit correlations across traces, but their performance depends on parameters such as rank, window size, and regularization coefficients. Signal leakage may occur in complex structures, under strong non-Gaussian erratic noise, or when the signal departs from the assumed low-rank model. Recent developments, including higher-order total-variation regularization and hybrid approaches, seek a better balance between noise suppression and amplitude fidelity [12, 13]. Nevertheless, these approaches still require researchers to specify priors, thresholds, ranks, or regularization parameters according to the data. When random and erratic noise coexist and overlap reflections in frequency or space, parameter sensitivity, applicability, and signal leakage remain persistent concerns [4, 9].

Deep learning provides a data-driven alternative to these approaches. Rather than relying on predefined filters, transform bases, or low-rank models, it learns nonlinear mappings from noisy seismic data to target data through training, reducing dependence on precise noise models and numerous manually specified parameters [1]. Recent seismic denoising networks have expanded both their representational capacity and their range of applications. Quadratic neurons have been used to improve the representation of complex seismic signals, while progressive multistage architectures have been developed to improve the preservation of weak reflections and shallow-layer features [14, 15]. Multiscale attention architectures provide another approach: Han et al. [16] combine multiscale feature extraction with dual-path attention to distinguish signals from background noise, while Yao et.al [17] integrate depthwise separable convolutions, channel attention, and residual dilated convolutions for efficient local feature extraction and multiscale context modeling. Combinations of diffusion models and principal component analysis, together with dual-domain Mamba architectures that model frequency information and long-range dependencies, offer further approaches to denoising under complex noise conditions [18, 19]. For settings with limited or no labels, researchers have also explored three-dimensional multiscale feature fusion, neural low-rank representations, and other self-supervised or unsupervised methods [20–23]. These studies demonstrate that deep learning can overcome some

limitations of conventional priors. However, increasingly complex architectures and diverse training strategies also make empirical model selection and experimental configuration more difficult. Performance differences across studies are often influenced jointly by training data, loss functions, learning rates, network depth, module combinations, and evaluation metrics. Proposing a new network alone therefore does not automatically resolve all practical challenges in seismic denoising.

Training data constitute the first challenge for data-driven deep-learning seismic denoising. Ideally, models should learn representative mappings between noisy data and noise-free targets, but field acquisition rarely provides strictly noise-free references. Survey areas also differ substantially in geological structure, acquisition systems, and noise distributions. Previous studies have expanded training samples using synthetic models with realistic structural characteristics or assembled larger pretraining datasets from multiple survey areas [24, 25]. Dataset construction thus determines which structural and noise conditions a model encounters and consequently influences generalization; it is more than a preliminary step before training. A second challenge concerns hyper-parameter selection. Although backpropagation automatically updates model parameters, choices of loss function, learning rate, dropout, network depth, and module configuration still require repeated experimentation. Their effects are often coupled: sequential selection or local adjustment may yield a suitable configuration for a particular dataset without establishing consistent performance for the target task. Studies of specialized networks and low-rank tensor models likewise show that architectural design and configuration require trade-offs specific to the data [14, 26]. Finally, performance gains without complete tuning records, module comparisons, and analysis of the underlying mechanisms provide limited evidence of why a model works or which design choices contribute to its performance. Data, mechanisms, and interpretability must also be considered when evaluating intelligent methods for industrial applications [26, 27]. The research need therefore extends beyond a more complex denoising network to a reproducible automated workflow connecting dataset construction, model configuration, architecture screening, and evidence recording.

To address these challenges, this study proposes an automated workflow covering the full development process for joint attenuation of random and erratic noise, with a focus on reducing reliance on manual expertise in dataset construction and network model configuration. Starting from parameterized three-dimensional synthetic seismic volumes, the workflow generates noise-free seismic responses by varying layered structures, folds, faults, and other geometric features within controlled ranges. It then selects informative samples from consecutive candidate sections according to differences in gradient-domain structure, reducing feature redundancy between adjacent sections. Paired noisy samples and labels are generated automatically by controlling random-noise intensity, the proportion of traces contaminated by erratic noise, and the spatial locations of that contamination. Sequential hyper-parameter tuning is performed within expert-constrained search spaces that include loss functions, hybrid-loss weights, learning rates, dropout rates, network depth, and network modules. Validation SNR serves as the primary evaluation metric, and training and validation results are recorded automatically at each stage. To address the sensitivity of squared-error losses to erratic noise, this study introduces a combination of adaptive Huber and

structural similarity losses. The former reduces the influence of high-amplitude outliers using thresholds estimated for each batch, while the latter adds constraints on reflection continuity and structural information. The hybrid-loss weight and relevant network modules are also selected by the workflow. Cumulative module screening is used to examine how different network structures contribute to denoising, ultimately yielding the U-shaped multiscale model MUnet within the specified search space. The workflow is evaluated quantitatively using SNR on synthetic data. The trained model is also transferred to the Stratton land and F3 marine three-dimensional seismic datasets, where section, difference-map, and spectral comparisons, together with quantitative local-similarity analysis, assess its behavior across acquisition environments and complex structures. Comparisons with the open-source Hankel sparse low-rank method (HSLR) and Seismic Adaptive Threshold Residual U-network (SATRNU) methods demonstrate the strong noise attenuation and signal-preservation capabilities of the MUnet model selected by the workflow. The central contribution is a reproducible, traceable automated workflow that constructs training datasets, tunes model hyper-parameters, and selects modules for the task while retaining complete records for subsequent performance comparisons and analysis of the underlying mechanisms.

The remainder of this paper is organized as follows. Section 2 describes the principles of the deep-learning denoising workflow, including dataset construction, network hyper-parameter tuning, and hybrid-loss design. Section 3 presents the training procedure and reports the denoising performance of the model obtained through the workflow on synthetic and field three-dimensional post-stack seismic data, with comparisons against other methods. Section 4 analyzes the mechanisms underlying each stage using the retained experimental records, further demonstrating the potential of the workflow for intelligent seismic denoising, and discusses its limitations and future research directions. Section 5 concludes the study.

2 Methodology

This study does not treat the simultaneous attenuation of random noise and erratic noise as a single network training problem. Instead, it formulates the task as a joint optimization workflow composed of problem definition, data construction, hyper-parameter search, and architecture screening. Given a noise-free seismic section $\mathbf{X} \in \mathbb{R}^{H \times W}$, the objective is to recover the effective signal from a noisy section $\mathbf{Y}$ while preserving event continuity and weak-reflection details. To this end, an automated workflow is constructed to generate training samples and labels automatically, sequentially optimize key hyper-parameters within a candidate space constrained by expert knowledge, and finally determine the network architecture for simultaneous attenuation of random and erratic noise. The core of this workflow is not to obtain a single optimal model from one training run, but to automatically record training and inference results under different configurations, thereby providing traceable experimental evidence for subsequent hyper-parameter sensitivity analysis and mechanistic discussion.

2.1 Problem Definition and Automated Dataset Construction

To characterize random noise and erratic noise simultaneously, the noisy seismic data are defined as:

$$\mathbf{Y} = \mathbf{X} + \mathbf{N} \tag{1}$$

where $\mathbf{X}$ is the noise-free effective signal, $\mathbf{N}$ denotes noise. Unlike conventional denoising tasks that target only one type of noise, this study must cover variations in noise intensity, spatial distribution, and outlier proportion during training. The training data therefore need sufficient diversity and controllability.

Constructing a training set directly from a limited amount of field data often leads to insufficient sample coverage, limited generalization ability, and restricted data access. To address this issue, this study adopts a synthetic data generation strategy based on parameterized geological structures and constructs the training set automatically in a programmatic manner. The generation of 3-D synthetic seismic volumes follows the idea of realistic structural model construction proposed by Wu et al. [24]: a layered reflection background is first generated from an impedance model, folds are then introduced through a vertical shear field, structural complexity is further enhanced through planar shear, fault structures with different strikes, dips, and displacements are subsequently superimposed, and the final noise-free seismic response is obtained by convolution with a Ricker wavelet. This workflow can continuously generate 3-D samples with different structural styles and geometric complexity within controllable parameter ranges, providing a unified basis for subsequent noise injection and network training.

During label construction, small blocks containing several consecutive sections are first extracted from the 3-D volume. Within each block, each candidate slice was firstly normalized by min-max scaling, and its Sobel gradient magnitude map was computed. The gradient-domain dissimilarity to the previously selected sample was then evaluated using $1 - \mathrm{SSIM}$ between the gradient magnitude maps, and the slice with the largest score was selected as the label sample. This criterion emphasizes differences in reflection geometry, discontinuities, and local texture while remaining simple to implement. The purpose is to reduce feature redundancy between adjacent sections and thereby improve the effective coverage of training samples. Specifically, the extraction direction of continuous slices is randomly selected by the program between inline and crossline to ensure that the network training contacts structural features along the survey line direction and perpendicular to the survey line direction at the same time, and avoids the introduction of directional bias due to single-directional slicing. Correspondingly, in the three-dimensional data inference stage, the model also supports slice prediction and reorganization along the inline or crossline direction, maintaining the consistency of the processing direction and the training distribution.

During sample construction, random noise is added to each label sample, and erratic noise is superimposed on a randomly selected subset of seismic traces to obtain a noisy sample paired with the corresponding label. By controlling random noise intensity, the proportion of traces contaminated by erratic noise, and their spatial locations, the automated workflow can generate training, validation, and test sets that cover different noise scenarios. The high-level procedure is summarized in Algorithm 1.

Algorithm 1: Automated dataset construction for simultaneous random and erratic noise attenuation

Input: Geological parameter ranges Ω_g, noise parameter ranges Ω_n, slice size (H, W) and candidate block depth K

Output: Training, validation, and test pairs $\mathcal{D} = \{(Y_n, X_n)\}$

$\mathcal{D} \leftarrow \emptyset$; `// Initialize dataset`

while *the target dataset size is not reached* **do**

  Generate a 3-D clean synthetic seismic volume V_c from Ω_g ;

  Extract a candidate block B with K consecutive inline or crossline slices from V_c ;

  Select the slice X with the largest dissimilarity to the previously accepted sample ;

  Add random noise and erratic noise into X according to Ω_n to obtain Y ;

  Append the pair (Y, X) to $\mathcal{D}$;

Split $\mathcal{D}$ into training, validation, and test subsets ;

return $\mathcal{D}$;

The automated procedure in Algorithm 1 converts a sample production process that previously depended on manual screening, cropping, and noise injection into a repeatable and scalable programmatic workflow. More importantly, dataset construction no longer serves only a single round of network training, but also provides unified and traceable experimental inputs for subsequent hyper-parameter tuning and architecture screening.

2.2 Automated Hyper-parameter Tuning Strategy

Network parameters can be updated automatically through the loss function and back-propagation, whereas hyper-parameters usually need to be preset before training and adjusted repeatedly according to experimental results. In the simultaneous attenuation of random noise and erratic noise, hyper-parameters affect not only convergence speed but also signal preservation, noise attenuation capability, and model interpretability. To reduce the time cost of trial-and-error tuning, this study adopts a sequential automated hyper-parameter tuning strategy that incorporates the loss function, dropout rate, learning rate, network depth, and network modules into a unified search process.

Let the set of hyper-parameters to be optimized be $\mathcal{H} = \{h_1, h_2, \ldots, h_K\}$, let the candidate set at stage k be $\mathcal{C}_k$, and let the optimal configuration obtained in the first $k-1$ stages be denoted by $\mathcal{H}^*_{k-1}$. The optimization objective at stage k can then be written as:

$$h^*_k = \arg\max_{h \in \mathcal{C}_k} Q\left(h \,\middle|\, \mathcal{H}^*_{k-1}\right) \tag{2}$$

where $Q(\cdot)$ denotes the validation performance metric that is computed automatically by the program while all other settings remain fixed. After the current stage is completed, the optimal result is passed to the next stage as the new baseline configuration.

In this way, the entire search process forms a recursive structure in which the best result from the previous stage constrains the search range of the next stage, rather than a one-shot parallel grid search. This strategy substantially reduces the search space while retaining the ability to investigate interactions among key hyper-parameters, thereby facilitating interpretation of different parts of the network.

For network module screening, this study further adopts a progressive cumulative ablation scheme instead of directly comparing all module combinations. Let the current baseline structure be $\mathcal{B}$ and the candidate module be m. The module retention criterion is written as:

$$\Delta Q_m = Q(\mathcal{B} \cup \{m\}) - Q(\mathcal{B}) \tag{3}$$

The module is retained when $\Delta Q_m > 0$; otherwise, it is removed. The result is therefore not merely a set of optimal numerical hyper-parameters, but an interpretable trajectory of architectural evolution. The corresponding sequential search procedure is summarized in Algorithm 2.

Algorithm 2: Sequential hyper-parameter auto-tuning under expert-constrained search ranges

Input: Training set $\mathcal{D}_{tr}$, validation set $\mathcal{D}_{val}$, Ordered hyper-parameter set $\mathcal{H} = \{\text{loss, dropout, learning rate, depth, modules}\}$, Candidate ranges $\mathcal{C} = \{C_1, C_2, \ldots, C_k\}$

Output: Optimized hyper-parameter configuration $\mathcal{H}^*$

Initialize the baseline configuration $\mathcal{H}^*$ using default or expert-constrained values ;

for $k = 1$ **to** K **do**

  Fix all hyper-parameters except h_k ;

  foreach *candidate* c *in* C_k **do**

    Train the network with $h_k \leftarrow c$ on $\mathcal{D}_{tr}$;

    Evaluate the validation metric $Q(c \mid \mathcal{H}^*)$ on $\mathcal{D}_{val}$;

    Record the training and validation results ;

  Update h_k in $\mathcal{H}^*$ using the candidate with the best validation performance ;

return $\mathcal{H}^*$;

Algorithm 2 embodies a sequentially inherited, rather than a parallel exhaustive, tuning strategy. The results from each stage are recorded automatically and passed to later stages, so the hyper-parameter search process itself can also serve as part of the mechanistic analysis.

2.3 Network Architecture

Because a U-shaped encoder-decoder architecture can capture a larger spatial context of seismic data and thereby extract informative features [28], this study adopts it as the basis and obtains the final MUnet shown in Fig. 1 through the automated workflow.

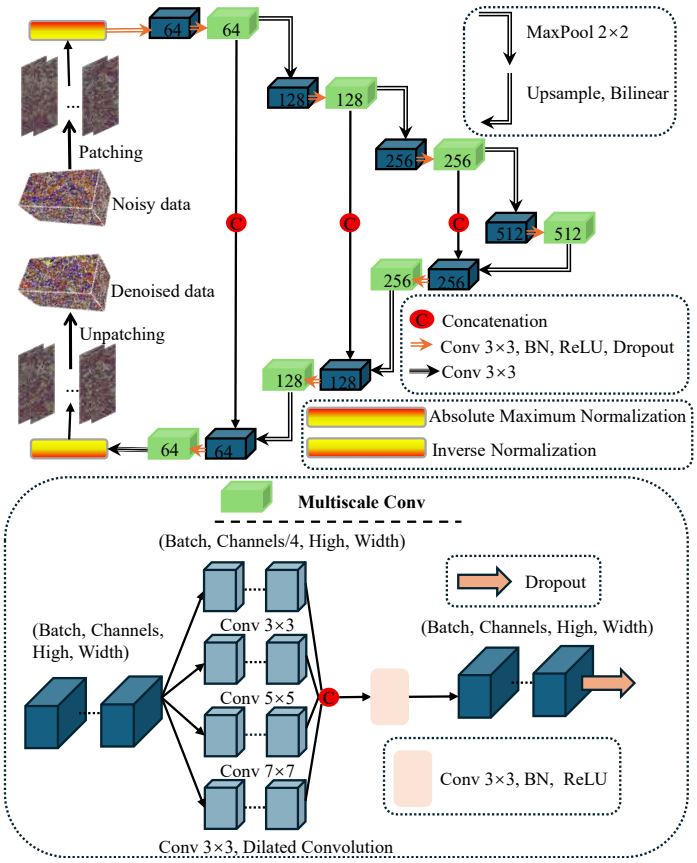

Fig. 1 Network architecture for simultaneous attenuation of random and erratic seismic noise under the automated workflow

Denote the overall network mapping by $f_\theta(\cdot)$. The training objective is:

$$\theta^* = \arg\min_\theta \frac{1}{N}\sum_{n=1}^{N}\mathcal{L}(f_\theta(\mathbf{Y}_n), \mathbf{X}_n) \tag{4}$$

where $\mathbf{Y}_n$ and $\mathbf{X}_n$ denote the nth noisy sample and its corresponding label, respectively, and $\mathcal{L}$ is the loss function to be optimized. In deep-learning-based seismic noise attenuation, the $L2$ loss gives relatively uniform emphasis and can reflect the distribution of prediction errors, which explains its widespread use compared with the $L1$ loss [29, 30]. However, the squared term in $L2$ amplifies the loss contribution of outliers and makes it sensitive to erratic values. The Huber loss combines the advantages of both and is therefore beneficial for this type of noise attenuation, although the choice of its threshold affects the final result [31]. For the error $e_{ij} = P_{ij} - X_{ij}$, the Huber function $\mathcal{F}_\delta(e_{ij})$ is defined as:

$$\mathcal{F}_\delta(e_{ij}) = \begin{cases} \frac{1}{2}e_{ij}^2, & |e_{ij}| < \delta, \\ \delta\left(|e_{ij}| - \frac{1}{2}\delta\right), & \text{otherwise.} \end{cases} \tag{5}$$

where the threshold δ is a fixed value determined from expert experience. Inspired by the superior performance of adaptive thresholds in the adaptive soft-thresholding module [32], this study abandons the use of a fixed threshold and determines δ dynamically according to the noise standard deviation σ in the current batch, so that the model can better handle the small amount of erratic noise in seismic data. Because accurate standard deviation calculation would substantially increase the training cost, the specific computation used here is:

$$\sigma_{\text{batch}} \approx \frac{\text{median}(|e_{\text{batch}} - \text{median}(e_{\text{batch}})|)}{0.6745} \tag{6}$$

that is, the median absolute deviation of the prediction error is used to estimate the standard deviation σ. At the same time, the coefficient 1.345 from [33] is used to define the dynamic threshold δ:

$$\delta = 1.345\,\sigma_{\text{batch}} \tag{7}$$

This yields the adaptive-threshold Huber loss $\mathcal{L}_{Adaptive-Huber}$, which improves model robustness in the presence of erratic noise in seismic data:

$$\mathcal{L}_{\text{Adaptive-Huber}} = \frac{1}{M \times N} \sum_{i,j} \mathcal{F}_\delta(e_{ij}) \tag{8}$$

where M and N denote the number of traces in the section and the number of sampling points per trace, respectively. Compared with natural image data in computer vision, seismic data exhibit stronger large-scale structural similarity, typically characterized by continuous events and layered distributions. The structural similarity index (SSIM) used in computer vision explicitly measures structural consistency. To constrain structural preservation, this study includes the adaptive Huber loss, the SSIM loss, and their hybrid form in the loss-function search space. The SSIM loss is defined as:

$$\mathcal{L}_{\text{SSIM}} = 1 - \text{SSIM}(\mathbf{P}, \mathbf{X}) \tag{9}$$

where the SSIM itself is defined as:

$$\text{SSIM}(\mathbf{P}, \mathbf{X}) = \frac{(2\mu_P\mu_X + C_1)(2\sigma_{PX} + C_2)}{(\mu_P^2 + \mu_Y^2 + C_1)(\sigma_P^2 + \sigma_X^2 + C_2)} \tag{10}$$

where μ_P and μ_X are the means of the predicted seismic data and the reference seismic data, respectively; σ_P^2 and σ_X^2 are their variances; σ_{PX} is their covariance; and the constant terms $C_1 = (K_1 L)^2$ and $C_2 = (K_2 L)^2$ prevent instability when the denominator approaches zero.

The hybrid loss constructed in this study can therefore be written as:

$$\mathcal{L}_{\text{Hybrid}} = \alpha\,\mathcal{L}_{\text{Adaptive-Huber}} + (1 - \alpha)\,\mathcal{L}_{\text{SSIM}} \tag{11}$$

where α, the SSIM window size, and the related parameters are all treated as part of automated hyper-parameter tuning. This design allows the loss function to suppress numerical deviations caused by outliers while constraining the continuity of seismic structures during training.

3 Experimental Results

This section presents the model training setup, synthetic-data results, and field-data results to verify the effectiveness and generalization of the proposed automated workflow for simultaneous attenuation of random noise and erratic noise, and to compare it with existing methods. All experiments were conducted on a workstation equipped with an Intel Core i5-12400F CPU and an NVIDIA GeForce RTX 4060 Ti GPU.

3.1 Experimental Setup

Considering GPU memory requirements and time cost, this study uses 2-D vertical sections to construct training samples for easier reproduction. In addition, deep learning methods depend heavily on training data. Because seismic data are expensive to acquire and involve regional privacy issues, recent studies have increasingly tended to use publicly available seismic data for testing [34–36]. Although Sheng et al. [25] collected 192 three-dimensional seismic datasets and constructed a 2-D dataset from them, this study uses only synthetic datasets for training and then transfers the resulting model directly to public field data for evaluation. This avoids overestimating model generalization when public real data are involved in training and testing and allows a more objective assessment of the effectiveness of the proposed workflow.

Following in Algorithm 1, the training data were generated by cutting consecutive section blocks of size $224 \times 224 \times 5$ from 3-D synthetic seismic volumes produced under different parameter combinations. From each block, the section with the largest difference from the previously selected sample was chosen as the label sample to reduce sample redundancy. The standard deviation range of random noise was set to $[0.001, 0.3]$, and the proportion of seismic traces randomly affected by erratic noise was set to $[0.05, 0.15]$. Strict separation of the training, validation, and test sets is enforced during the sample generation stage. These subsets are independently generated via geological structure and noise parameters controlled by distinct random seeds, precluding any sample overlap or potential information leakage. The final training, validation, and test sets contained 1600, 200, and 200 pairs of 2-D vertical sections, respectively. Representative automatically generated samples are shown in Fig. 2.

In addition, the network depth is jointly constrained by the input data size and the convolution kernel size, and the maximum network depth for continuous downsampling is set to 5. Specifically, since there is a multi-scale module with 7×7 size convolution kernel in the module hyper-parameter selection of the subsequent network structure, and the training data with size 224×224 is input into the network and subjected to 5 times of maximum pooling downsampling, it becomes a feature map reduced to 7×7 size. If the feature map size is further reduced, the scale matching relationship with the convolution kernel will be destroyed. Therefore, in the hyper-parameter candidate

space of the automated workflow, the upper limit of the network depth of continuous downsampling is set a priori to 5 layers.

The fact that the upper limit of network depth stabilizes at five layers is not accidental, but is instead a structural constraint jointly determined by the input size of 224×224 and the scale of the multiscale convolution kernels. After five rounds of consecutive downsampling, the spatial resolution of the feature map is compressed to 7×7, which matches the largest convolution-kernel scale in the multiscale module. In addition, for the SSIM loss function in 9, because this study applies maximum absolute-value normalization to the seismic data, the dynamic range of the data is scaled to $[-1, 1]$, so the dynamic-range parameter is $L = 2$. Although the computer-vision literature usually takes $K_1 = 0.01$ and $K_2 = 0.03$, this study predefined the ranges of K_1 and K_2 in the automatic hyper-parameter tuning process and allowed the Algorithm 2 to search for their optimal values, so as to examine more closely the suitability of this parameter configuration for seismic-noise attenuation.

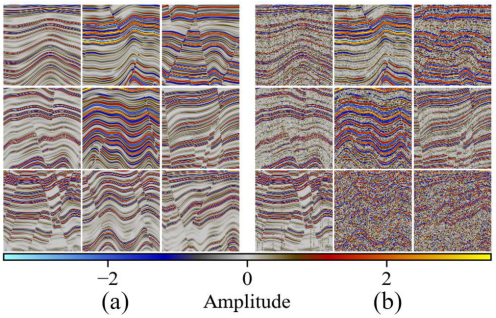

Fig. 2 Representative synthetic sample pairs generated by the automated dataset construction workflow. (a) Inline or crossline slices extracted from the 3-D synthetic seismic volumes. (b) Corresponding noisy samples with random and erratic noise contamination.

Before training, the input data were scaled to the interval $[-1, 1]$ by maximum absolute-value normalization to reduce the influence of amplitude-scale differences among samples on training stability and to match the amplitude distribution characteristics of seismic data [37]. During training, the process was stopped when either the validation loss or the training loss failed to decrease for 10 consecutive epochs, so as to avoid overfitting or underfitting under limited seismic samples. Dropout was treated as a regularization component and jointly optimized with the learning rate, network depth, and module structure in the hyper-parameter search, whereas the number of training epochs itself was determined adaptively by early stopping.

During inference, to avoid stitching artifacts at the boundaries of 2-D vertical sections, this study adopted overlapping sliding-window prediction. The stride was set to 3/4 of the patch size, corresponding to an overlap ratio of 1/4, to balance inference efficiency and boundary continuity [38]. For 3-D seismic volumes, inference and reassembly were carried out along the seismic vertical profile, corresponding to the patching and unpatching processes in Fig. 1. In this way, although the network

was trained on 2-D sections, it can still be applied rapidly to 3-D seismic data while maintaining low GPU memory requirements.

Although the automated workflow proposed in this study greatly facilitates deep-learning-based denoising research and allows researchers to focus on the interpretability and effectiveness of network models for seismic noise attenuation, a comparative analysis with different advanced methods is still necessary in order to present objectively the noise attenuation performance achieved by the automatically selected hyper-parameters and dataset construction scheme in this study. To ensure reproducibility, two open-source advanced methods were selected as baselines: the SATRNU, known for its lightweight design and inference efficiency [39], and the HSLR, which improves sparse low-rank Hankel approximation through a multivariate extension of the minimax concave penalty function [11].

For synthetic data, the signal-to-noise ratio (SNR) formula given in [40] was used as the quantitative evaluation metric:

$$\mathrm{SNR} = 10\lg\frac{\sum_{i=1}^{M}\sum_{j=1}^{N}s_{ij}^{2}}{\sum_{i=1}^{M}\sum_{j=1}^{N}(s_{ij}-\eta_{ij})^{2}} \tag{12}$$

where s_{ij} is the amplitude of the noise-free data and η_{ij} is the amplitude of the noisy or denoised data. For field data, because no noise-free ground truth is available, local similarity is widely used to assist in evaluating the degree of effective signal leakage [41, 42]. Its value ranges from 0 to 1 and is positively related to the intensity of effective signal leakage, with lower values indicating less energy leakage [9]. To calculate signal leakage accurately for 3-D data, the local-similarity parameters were set in strict accordance with the standards in the public code example, namely $rect = [5, 5, 5]$ and $niter = 20$. The mean local similarity was denoted by LS_{avg}.

3.2 Synthetic Data Results

One strongly contaminated sample and one weakly contaminated sample were selected as representative results, corresponding to Fig. 3 and Fig. 4, respectively.

Under strong noise interference, the three methods show clear differences. Fig. 3(j) shows that, after HSLR denoising, substantial random disturbances remain across the full frequency band, and Fig. 3(d) indicates that continuity recovery for faults and horizons is limited. SATRNU can reduce the noise background substantially, but some structural blurring remains at local strong reflections and fault intersections. MUnet, by contrast, shows clearer reflection continuity and more complete noise separation. Its SNR is higher than those of HSLR and SATRNU, and the spectral result in Fig. 3(j) shows that the green average-amplitude curve of MUnet is closest to the gray noise-free reference curve, indicating that it attenuates both low-frequency and high-frequency noise while preserving effective information in the main frequency band. However, the loss of effective signals is difficult to observe directly from the three residual sections in Fig. 3(g), Fig. 3(h), and Fig. 3(i). Another sample with weaker noise interference was therefore selected for further analysis.

Under weaker noise interference, all three methods achieve some degree of noise attenuation, but the differences in effective-signal preservation become clearer. Fig.

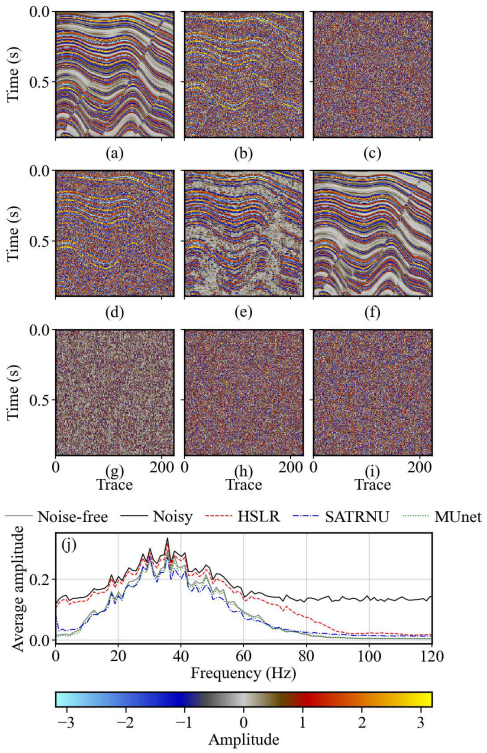

Fig. 3 Synthetic example under severe noise contamination. (a) Noise-free reference. (b) Noisy input with SNR = -1.18 dB. (c) Added noise. (d)–(f) Denoised results of HSLR, SATRNU, and MUnet, with SNR of 1.66 dB, 7.08 dB, and 13.74 dB, respectively. (g)–(i) Corresponding residual maps. (j) Average amplitude spectra.

4(g) and Fig. 4(h) show that both HSLR and SATRNU exhibit obvious effective-reflection leakage, especially in strong-reflection regions. By contrast, the residual in Fig. 4(i) for MUnet is dominated mainly by random noise components. The spectral comparison in Fig. 4(j) further shows that SATRNU suppresses energy more strongly in the mid- and high-frequency bands, whereas the spectra of HSLR and MUnet are closer to the original noise-free data, with MUnet performing better in both overall curve agreement and structural continuity. The corresponding SNR results also show that MUnet is clearly superior to HSLR and SATRNU. Taken together, Fig. 3 and Fig. 4 show that MUnet maintains a more stable advantage under both strong-noise and weak-noise conditions, indicating that the optimal configuration obtained by the automated workflow is not limited to a single noise level. Fig. 5 further evaluates the robustness of MUnet under different degrees of noise interference. It shows that, whether the seismic data are contaminated by strong noise or weak noise, MUnet consistently delivers the best noise attenuation performance.

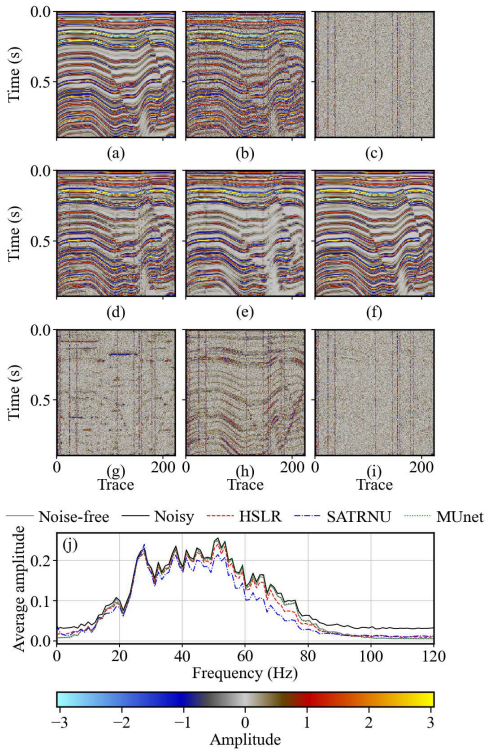

Fig. 4 Synthetic example under relatively weak noise contamination. (a) Noise-free reference. (b) Noisy input with SNR = 9.27 dB. (c) Added noise. (d)–(f) Denoised results of HSLR, SATRNU, and MUnet, with SNR of 12.95 dB, 10.19 dB, and 20.26 dB, respectively. (g)–(i) Corresponding residual maps. (j) Average amplitude spectra.

3.3 Field Data Results

The effect of this automated workflow has already been reflected on the untrained synthetic seismic test set. However, both the synthetic test set and the training set were generated from the same synthetic-data generation theory and differ only in the parameter coefficients of reflection coefficients, folds, faults, and noise. To further examine generalization, the model trained only on synthetic-data features was applied to the Stratton 3D onshore dataset from the United States. This avoids information leakage caused by including field data in training and provides a stricter evaluation of how well the model generalizes when transferred from synthetic samples to real scenarios. The Stratton 3D dataset has dimensions of $(1501, 309, 230)$ with a sampling interval of 2 ms.

The results in Fig. 6(c), Fig. 6(f), and Fig. 6(i) show that SATRNU suffers from severe effective-signal leakage. By contrast, MUnet shows only weak effective-signal leakage, as illustrated in Fig. 6(d), Fig. 6(g), and Fig. 6(j). HSLR, however, exhibits obvious effective-signal leakage only in the shallow part, while leakage in the deeper strata is not obvious, as shown in Fig. 6(b), Fig. 6(e), and Fig. 6(h), and it also yields the lowest overall mean local similarity. Because image-based visualization of the full

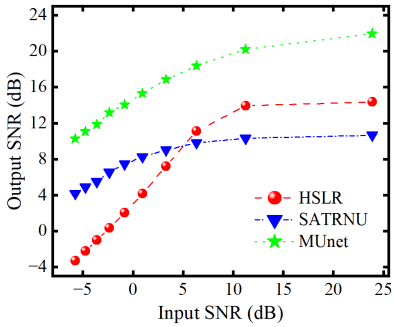

Fig. 5 Robustness test results under different noise levels.

Stratton 3D volume does not show local details clearly enough, the inline 200 section was further extracted to compare local structural preservation and spectral variation more clearly. The results are shown in Fig. 7. Fig. 7 shows that HSLR has the amplitude spectrum closest to the original data, but the enlarged view in Fig. 7(b) indicates that obvious noise still remains in the section. This means that its lower local similarity is achieved at the expense of insufficient denoising rather than stronger noise attenuation capability. SATRNU restores more continuous events, but Fig. 7(f) and Fig. 7(i) reveal stronger effective-signal loss. MUnet reaches a more reasonable balance between the two: its denoised section has a substantially reduced noise background in Fig. 7(d), both strong and weak reflections retain good continuity, and the difference map in Fig. 7(g) and the local similarity map in Fig. 7(j) also show that its effective-signal leakage is clearly lower than that of SATRNU. For the Stratton data, MUnet achieves the best overall balance between denoising capability and effective-signal leakage.

The results on the onshore 3-D seismic dataset already show that MUnet can attenuate noise effectively and performs strongly in terms of event continuity and effective-signal preservation in both shallow and deep sections. This study further selected a public subset of the F3 block for testing. The data volume has dimensions of $(450, 600, 810)$ with a sampling interval of 4 ms. This block has undergone preliminary denoising, but some noise still remains, making it more suitable for evaluating the ability to distinguish high-quality results. Comparisons for the full 3-D result and the inline 200 section are shown in Fig. 8 and Fig. 9, respectively.

Consistent with the observations on the Stratton data, Fig. 9(b) shows that HSLR on the F3 data also produces relatively small modifications but leaves more residual noise, indicating limited attenuation capability for complex field noise. In structurally complex regions of the F3 data, especially near uplifts, faults, and anticlines in Fig. 9(c), the difference map in Fig. 8(f), Fig. 9(f) and the local similarity map in Fig. 8(i), Fig. 9(i) all indicate more obvious effective-signal loss for SATRNU. By contrast, MUnet achieves clear noise attenuation on the F3 data in Fig. 8(d), Fig. 9(d), while preserving key structural boundaries and local reflection continuity well. The spectrum in Fig. 9(k) also shows that, unlike SATRNU, MUnet does not introduce stronger spectral-amplitude deviations over a wide frequency band, but maintains a more reasonable amplitude distribution while effectively suppressing noise. These results indicate that the optimal model obtained by the proposed automated workflow

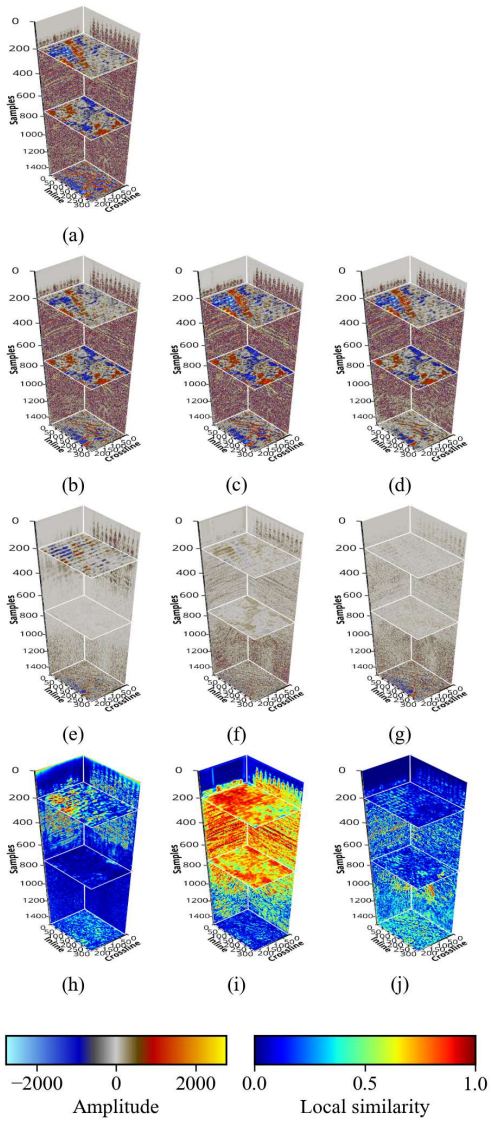

Fig. 6 Comparison on the Stratton field data. (a) Original volume. (b)–(d) Denoised results of HSLR, SATRNU, and MUnet. (e)–(g) Difference between the original data and denoised results. (h)–(j) Local similarity maps, with LS_avg of 0.153, 0.594, and 0.262, respectively.

can not only be transferred to field data acquired under different environments, but also retain good structural preservation in complex structural regions.

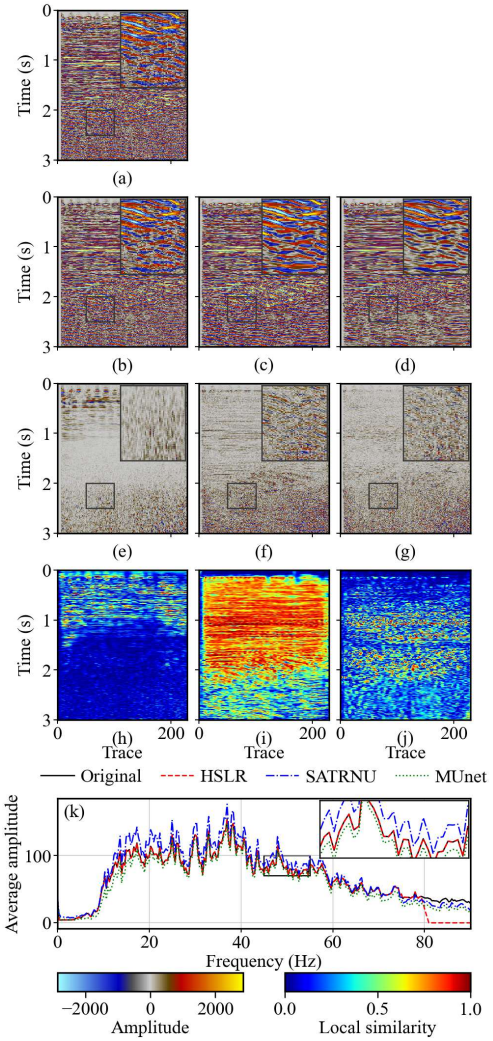

Fig. 7 Comparison on the Stratton data inline 200. (a) Original volume. (b)–(d) Denoised results of HSLR, SATRNU, and MUnet. (e)–(g) Difference between the original data and denoised results. (h)–(j) Local similarity maps.

3.4 Summary

The experimental results in this section show that the proposed automated workflow maintains stable advantages on both synthetic data and public field data. For synthetic data, MUnet achieves the highest SNR under both strong-noise and weak-noise conditions and shows better signal-preservation capability in both the residual maps and the spectra. For the Stratton and F3 onshore and offshore field datasets, MUnet reaches a better balance between noise suppression and effective-signal preservation, as indicated jointly by the difference maps, local enlarged views, and amplitude-spectrum analysis. This fully demonstrates that the automated workflow proposed in this study

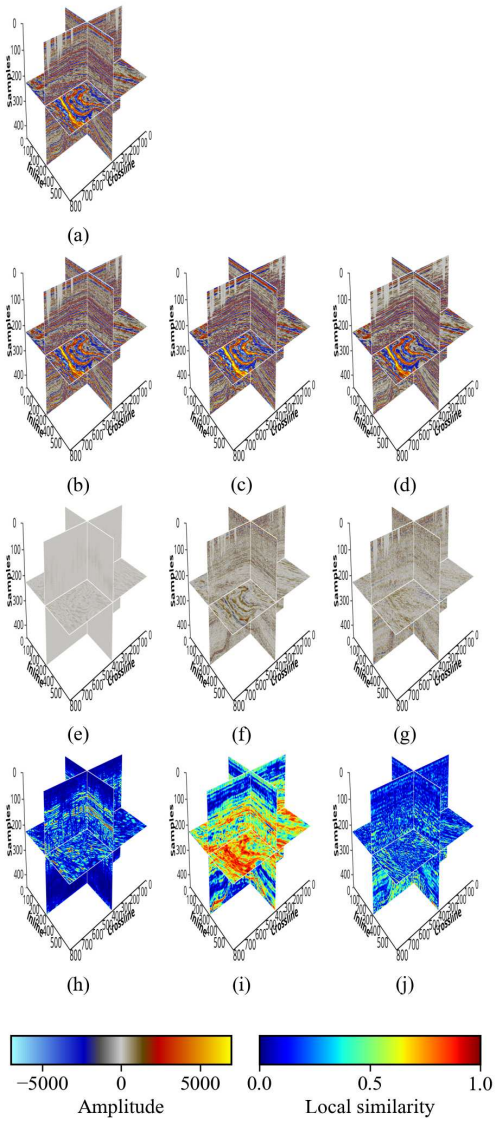

Fig. 8 Comparison on the F3 field dataset. (a) Original volume. (b)–(d) Denoised results of HSLR, SATRNU, and MUnet. (e)–(g) Difference volumes. (h)–(j) Local similarity maps, with LS_avg of 0.137, 0.446, and 0.208, respectively.

can automatically obtain a seismic-noise attenuation network model with superior performance.

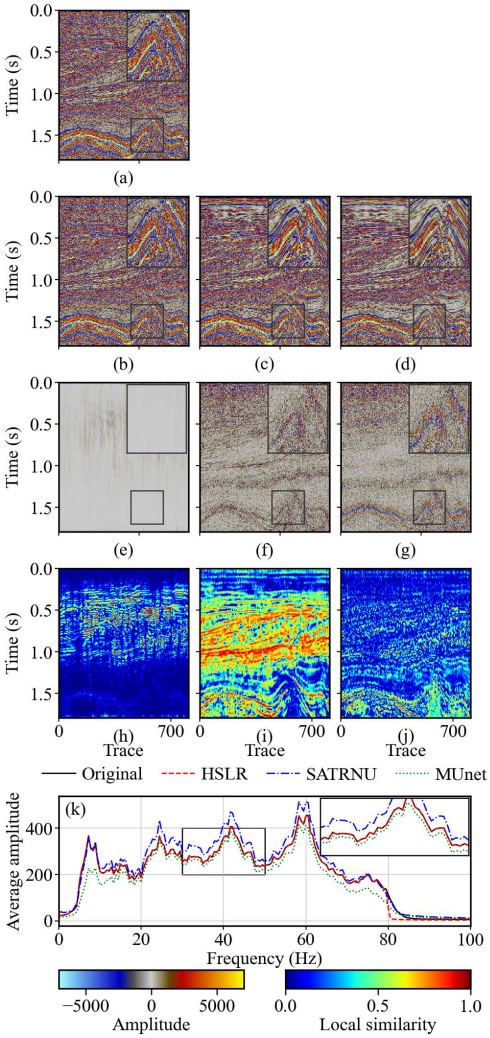

Fig. 9 Comparison on inline 200 of the F3 data. (a) Original profile. (b)–(d) Denoised results of HSLR, SATRNU, and MUnet, respectively. (e)–(g) Difference maps. (h)–(j) Local similarity maps. (k) Average amplitude spectra. Insets indicate enlarged local regions.

4 Discussion

Based on the comparative experimental results on synthetic and field data, together with the complete records of automatic hyper-parameter tuning, this study characterizes the effective mechanism of the automated workflow as the synergy between automated dataset construction and sequential hyper-parameter optimization. The following discussion analyzes the mechanism from three aspects, namely dataset construction, hyper-parameter optimization strategy, and the final network model,

Table 1 Processing time consumption and mean local similarity of each method

Method	Processing time/s			Mean local similarity/dB		
	Stratton data	F3 data	Synthetic data section	Stratton data	F3 data	Synthetic data section
HSLR	2792.78	29807.16	59.995	**0.153**	**0.137**	0.194
SATRNU	**16.90**	**28.66**	**0.006**	0.594	0.446	0.244
MUnet	92.12	152.55	0.015	0.262	0.208	**0.119**

Note: Bold values indicate the best results under different conditions

and then discusses the current limitations of the workflow and directions for future development.

4.1 Mechanisms Behind the Automated Dataset Construction

The reason why automated dataset construction can support strong performance on both synthetic and field data is not simply that it enlarges the number of samples, but that it systematically improves structural diversity, noise diversity, and the effective density of samples. Specifically, the training samples are generated from parameterized three-dimensional geological structure models. Different fold patterns, fault combinations, and reflection-coefficient configurations expose the network during training to a broader range of geometric forms and texture variations. This idea is consistent with the mechanism by which automatically generated realistic structural models contribute to seismic interpretation tasks [24]. At the noise level, the intensity of random noise, the proportion of erratic noise, and its spatial distribution are all controlled programmatically. What dataset automation truly expands, therefore, is the observable input-condition space of the network rather than merely replacing manual noise injection.

Another key dimension of this mechanism lies in redundancy control. Adjacent seismic sections are highly similar spatially. If two-dimensional samples are obtained simply by random cropping, the training set can still contain statistically repetitive coverage even when the total number of samples increases. This study adopts a selection rule that prioritizes the sample with the largest difference within each consecutive small block. In essence, this increases the information density of the samples under fixed storage and computational budgets. The result is not an increase in the total number of samples, but an increase in the marginal contribution of each sample to the training objective. The experimental results in the previous section show that this sample-selection strategy is sufficient to support successful transfer of the model to the Stratton and F3 public three-dimensional datasets using only 1600 pairs of two-dimensional samples for training. This indicates that the automated data workflow improves the effective coverage of the training distribution rather than mechanically expanding the sample scale.

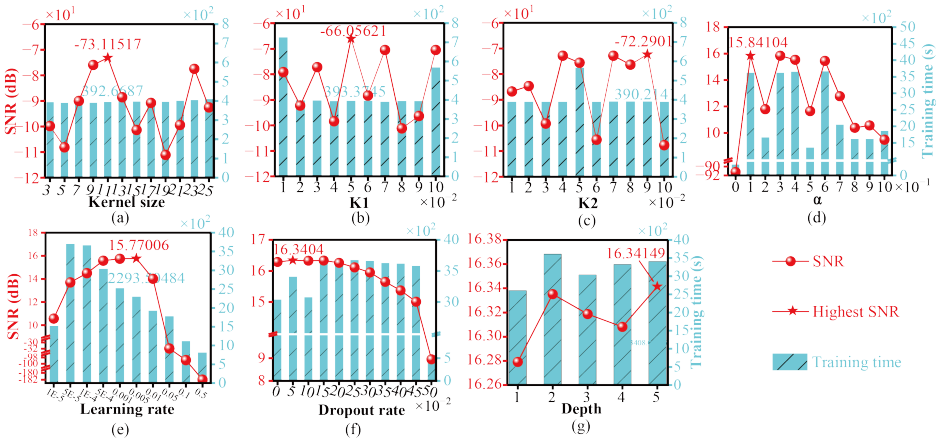

Fig. 10 Hyper-parameter auto-tuning records. Panels (a)–(g) report the effects of SSIM window size, K_1, K_2, loss weight α, learning rate, dropout rate, and the number of multiscale layers, respectively. Some coordinate axis ticks have been scaled by order of magnitude, and all numerical values within the plotting area retain their unscaled raw data values.

From the perspective of engineering practice, data automation also substantially alleviates the hidden time cost in obtaining a model. Table 1 reports inference time rather than the total time required for model acquisition. In practical work, however, model acquisition is often constrained first by the data-preparation stage rather than by forward propagation itself. Many recent methods still rely on strategies such as synthetic data, transfer learning, or inference after pretraining when ground-truth labels for field data are unavailable [18, 43]. The advantage of the present workflow is that it pushes these steps further upstream into a repeatable and standardized procedure, so that subsequent network training, hyper-parameter comparison, and architecture screening are all built on the same automatically generated data basis. This is also an important prerequisite that allows this study to compare different hyper-parameters systematically rather than merely presenting the result of a single optimal model.

4.2 Mechanisms Behind Sequential Hyper-parameter Optimization

Artificial-intelligence methods in geophysics have long faced the difficulty of limited model interpretability. The automated workflow proposed in this study constrains the search space of each hyper-parameter within ranges defined by expert experience and records the complete tuning trajectory of every parameter, thereby providing a systematic analytical tool for investigating the role and physical meaning of different network components. At the same time, sequential automated hyper-parameter tuning converts what would otherwise be a strongly coupled, high-dimensional joint search problem into a staged decision process that can be inherited, compared, and recorded. If all hyper-parameters were searched by parallel exhaustive enumeration, not only would the computational cost be extremely high, but it would also be difficult to

Table 2 Automatic tuning records of network modules

Module Name	SNR (dB)	Retention	Training Time (s)	Params (MB)	FLOPs (GB)	Memory Usage (GB)	
						Inference	Training
CDM	-26.3801	No	**1415.46**	6.72	23.18	0.22	1.02
CUM	14.7275	No	4263.94	**5.86**	27.23	**0.11**	**0.56**
CBAM	15.6988	No	11493.62	6.83	**21.81**	0.23	1.13
MFM	**16.6494**	**Yes**	21209.41	17.14	56.36	2.20	2.66
ASM	16.0385	No	22810.72	18.01	56.37	2.20	2.79

Note: The initial baseline is the average signal-to-noise ratio on the validation set (16.3415 dB) after updating the optimal solution of hyper-parameter C_{k-1} in Algorithm 2. Because the signal-to-noise ratio of the multiscale feature module is higher than the initial baseline, it replaces the latter as the new baseline.

determine which factor actually dominates a given performance change. The sequential strategy adopted here passes the best result from each stage to the next, giving the search process clear conditional boundaries and thus providing direct evidence for subsequent mechanistic analysis. Therefore, beyond the basic hyper-parameters needed to ensure network convergence, this study focuses its analysis on the mechanisms by which the loss function and network modules affect attenuation of random noise and erratic noise. The loss function and network modules are accordingly set as C_1 and C_k, namely the first and last optimization stages, in the automated hyper-parameter workflow of Algorithm 2. The records of the entire tuning process are shown in Fig. 10.

Fig. 10 shows that when the SSIM loss is used alone, even after its window-size parameter is optimized automatically, the signal-to-noise ratio on the validation set still does not improve, and the training process terminates early after a short period. This indicates that structural-similarity constraints alone are insufficient for joint attenuation of random noise and erratic noise. When SSIM is combined with the adaptive Huber loss, however, the result is better than that obtained with the adaptive Huber loss alone, since $\alpha = 1$ in the hybrid loss reduces the latter to the adaptive Huber loss. These results show that the adaptive Huber loss suppresses high-amplitude outliers through a dynamic thresholding mechanism within each batch, making the model more robust to erratic noise, whereas the SSIM term provides a supplementary constraint for preserving event continuity and layered structure. When combined, the hybrid loss retains robustness to outliers while introducing an explicit preference for structural information. This behavior is consistent with recent studies that compensate for the limitations of a single loss by incorporating noise-level estimation, multistep inference, or explicit prior embedding [18, 26]. Unlike those works, the relevant parameters in this study are all optimized automatically by the automated workflow without requiring repeated manual trial and error.

4.3 Mechanisms Behind the Final Network Configuration

In the network-module screening stage of Algorithm 2, the highest mean signal-to-noise ratio on the validation set was again used as the criterion to determine sequentially whether each module effectively attenuated noise and should therefore be retained. The tuning range included the Convolutional Block Attention Module (CBAM), which suppresses redundant background features at both spatial and channel levels; the Multiscale Feature Module (MFM), which captures waveform and structural features at different scales through parallel convolution kernels; the Adaptive Soft-threshold Module (ASM), which is sensitive to anomalous responses; Convolution-based Downsampling Module (CDM) and Convolution-based Upampling Module (CUM) replacements for simple pooling downsampling and bilinear-interpolation upsampling, respectively. The tuning records are shown in Table 2.

Table 2 shows that the multiscale feature fusion module is the only module retained. This result is not merely an empirical observation that multiscale modules are effective. Rather, it can be attributed to the basic characteristics of the task of simultaneous attenuation of random noise and erratic noise. Random noise usually appears as more dispersed high-frequency disturbances and requires a larger receptive field to distinguish it statistically from effective structures. Erratic noise, by contrast, often appears as local high-amplitude anomalies and requires a smaller receptive field to identify its local discontinuity from normal reflection events. Multiscale fusion preserves lateral continuity, local abrupt changes, and vertical layered relationships simultaneously within the same network. This conclusion is also consistent with the performance of three-dimensional multiscale feature fusion methods in random-noise suppression tasks [20]. In addition, Table 2 shows that basic downsampling and upsampling modules are structural prerequisites for this task. The more complex modules used to replace them produced signal-to-noise ratios far below the baseline value, indicating that complex architectures cannot substitute for simple hierarchical representation and progressive reconstruction mechanisms. This agrees with recent multistage progressive networks that emphasize the sustained transfer of hierarchical features [15].

It is worth noting that neither CBAM, which is designed to enhance salient feature responses, nor adaptive soft threshold modules, which are more directly oriented to suppressing anomalies, are retained in this automated workflow. This result indicates that, on the basis of the hyper-parameter tuning already completed in Algorithm 2, the additional information gain provided by these two types of modules is lower than the complexity and training cost they introduce. In other words, these negative module-selection results are also interpretable: in the task of simultaneous attenuation of random noise and erratic noise, the decisive improvement comes from multiscale representation capability rather than the simple stacking of all enhancement modules. This also helps explain why some new networks that emphasize global context, frequency-domain information, or physical-prior embedding may each have their own advantages, yet still need to answer the more fundamental question of which type of information is truly dominant [19, 26].

4.4 Limitations and Implications

Although the three mechanisms discussed above explain the effectiveness of the present workflow, the discussion also reveals several unavoidable boundary conditions. Automated tuning based solely on the signal-to-noise ratio as the evaluation criterion does not mean that computational cost can be ignored. Table 1 shows that the final MUnet still shortens inference time by more than one order of magnitude compared with HSLR on both field datasets, but remains slower than the lightweight SATRNU. This indicates that the tuning process, when optimized only for the signal-to-noise ratio, pursues maximum accuracy while overlooking time cost, even though both efficiency and performance are important considerations in practical industrial applications. Similarly, the KAN low-rank network, which emphasizes efficient representation, also treats efficiency as a goal that is as important as performance [21]. In addition, sequential hyper-parameter optimization is essentially still a conditional optimal search rather than a global optimal search. If the traversal order of the hyper-parameters changes, the baseline configuration inherited by later stages also changes accordingly, so the final result remains path dependent. Moreover, to test generalization ability strictly on public data, this study did not introduce any public data samples during dataset construction. Although transfer from synthetic training to field testing performs well, an unavoidable distribution gap still remains between the synthetic domain and the real domain.

These limitations also point directly to future development of the workflow. At the optimization-strategy level, multi-objective optimization or Bayesian search may be introduced so that the search process can balance signal-to-noise ratio, fidelity, effective-signal loss, inference time, and memory cost simultaneously rather than relying on a single metric. At the architectural level, further exploration may be directed toward network designs with stronger representational ability while still preserving interpretable boundaries, such as the structural potential shown by dual-encoder models and implicit neural representations [43]. At the data level, domain adaptation, semi-supervised learning, or self-supervised fine-tuning strategies for field data may be introduced to build a closer link between automated synthetic samples and real-noise characteristics. From a broader geophysical perspective, the real significance of the present workflow lies not only in seismic denoising itself, but also in the complete methodological route it provides: automatic data construction, automatic network comparison, and automatic evidence retention. The same route can also be transferred to tasks such as first-break picking, horizon tracking, fault detection, and reservoir prediction, in which case only the sample-construction scheme and the model-evaluation metrics need to be redefined according to the specific task.

5 Conclusion

This study develops an automated workflow for joint attenuation of random and erratic seismic noise, integrating synthetic dataset construction, sequential hyper-parameter tuning, and network module selection. By generating diverse paired samples, screening configurations within expert-constrained search spaces, and automatically retaining experimental records, the workflow reduces repetitive manual work throughout

model development. The selected MUnet achieves higher output SNR than HSLR and SATRNU across the tested synthetic noise levels. On the Stratton land and F3 marine three-dimensional seismic datasets, quantitative local-similarity analysis, together with section, difference-map, and amplitude-spectrum comparisons, demonstrates effective noise attenuation and reflection preservation. These results show that the workflow can obtain an effective denoising model using synthetic training data and support its application to field data across different acquisition environments.

Analysis of the retained records indicates that adaptive Huber and SSIM losses provide complementary constraints: batch-wise Huber threshold estimation reduces sensitivity to high-amplitude erratic noise, while SSIM promotes structural continuity. Automatic selection of their relative weight removes the need for repeated manual trials, and module screening identifies multiscale feature fusion as an effective design choice for this task. Researchers can extend the candidate set with new network architectures or modules and use the same workflow for automated evaluation and selection, with complete records supporting subsequent performance comparisons and analysis of the underlying mechanisms. Publicly available data and open-source code facilitate independent reproduction, shared benchmarking, and collaborative development. Together, these capabilities provide practical value and opportunities for further applications in seismic processing. The current workflow remains subject to search-order dependence, a single selection metric, and differences between synthetic and field data. Future work can address these issues through multi-objective optimization, domain adaptation, and stronger structural representations.

Code availability. Name of code: automated-seismic-denoising-workflow. The source code is available at https://github.com/fathercharose/automated-seismic-denoising-workflow.

Funding. This work was supported by the Scientific Research and Technology Development Project of China National Petroleum Corporation (Grant No. 2021DJ3704, "High-Resolution Seismic Prediction Technology for Thin Reservoirs"); and the Open Fund of Key Laboratory of Exploration Technologies for Oil and Gas Resources (Yangtze University), Ministry of Education (Grant No. K2024-22).

Competing interests. The authors declare that they have no known competing financial interests or personal relationships that could have appeared to influence the work reported in this paper.

Data availability. Implementations of the two benchmark methods, SATRNU and HSLR, are available at https://github.com/fathercharose/SATRNU and https://github.com/mokhtarmohammadi/HSLR, respectively. The synthetic seismic datasets used in this study are available from IEEE DataPort at https://doi.org/10.21227/708y-pk42. The Stratton 3D land seismic data are available at https://wiki.seg.org/wiki/Stratton_3D_survey, and the F3 marine 3D seismic data are available at https://terranubis.com/datainfo/F3-Demo-2023.

Author contribution. Mingde Chen: Conceptualization, methodology, validation, formal analysis, investigation, resources, data curation, software, visualization, and

writing. Rui Guo: writing, formal analysis, and data curation. Aohuai Pan: validation, investigation, and methodology. Chen Li: software, resources, and validation. Wei Chen: conceptualization and investigation. Zhixian Gui: supervision, project administration, and funding acquisition. All authors reviewed and approved the manuscript.

Declaration of generative AI and AI-assisted technologies. During the preparation of this work, the authors used Codex (OpenAI) solely for translation. After using this tool, the authors reviewed and edited the manuscript as needed and take full responsibility for the content of the publication.

References

[1] Yu, S., Ma, J. & Wang, W. Deep learning for denoising. *Geophysics* **84**, V333–V350 (2019).

[2] Cui, Y. *et al.* Research progress of random noise attenuation methods for seismic data based on deep learning. *Oil Geophysical Prospecting* **58**, 1269–1283 (2023).

[3] Jeong, W., Almubarak, M. S. & Tsingas, C. Seismic erratic noise attenuation using unsupervised anomaly detection. *Geophysical Prospecting* **69**, 1473–1486 (2021).

[4] Chen, K. & Sacchi, M. D. Robust reduced-rank filtering for erratic seismic noise attenuation. *Geophysics* **80**, V1–V11 (2015).

[5] Sternfels, R., Viguier, G., Gondoin, R. & Le Meur, D. Multidimensional simultaneous random plus erratic noise attenuation and interpolation for seismic data by joint low-rank and sparse inversion. *Geophysics* **80**, WD129–WD141 (2015).

[6] Oboué, Y. A. S. I., Chen, Y., Bai, M., Chen, W. & Chen, Y. Erratic and random noise attenuation using adaptive local orthogonalization. *Geophysics* **87**, V381–V396 (2022).

[7] Liu, G., Liu, Y., Li, C. & Chen, X. Weighted multisteps adaptive autoregression for seismic image denoising. *IEEE Geoscience and Remote Sensing Letters* **15**, 1342–1346 (2018).

[8] Ahmed, F. Y., Almubarak, M. & Tsingas, C. Applications of seislet transform and signal and noise orthogonalization to seismic data from the middle east. *Journal of Applied Geophysics* **161**, 193–203 (2019).

[9] Chen, Y. & Fomel, S. Random noise attenuation using local signal-and-noise orthogonalization. *Geophysics* **80**, WD1–WD9 (2015).

[10] Huang, W., Wang, R., Chen, Y., Li, H. & Gan, S. Damped multichannel singular spectrum analysis for 3d random noise attenuation. *Geophysics* **81**, V261–V270 (2016).

[11] Anvari, R. *et al.* Random noise attenuation in seismic data using hankel sparse low-rank approximation. *Computers & Geosciences* **153**, 104802 (2021).

[12] Zhang, P. *et al.* Amplitude-preserving 3-d TV regularization for seismic random noise attenuation. *IEEE Geoscience and Remote Sensing Letters* **22** (2025).

[13] Wang, S., Liu, Y., Li, X., Lin, P. & Gao, L. Random noise suppression of seismic data based on ceemd-mssa. *Journal of Mining Science and Technology* **11**, 103–113 (2026).

[14] Wang, X., Sui, Y. & Ma, J. Quadratic unet for seismic random noise attenuation. *Geophysics* **90**, V53–V65 (2025).

[15] Li, G., Li, H., He, S. & Wang, L. Multi-stage progressive network for seismic random noise suppression. *Journal of Seismic Exploration* **34**, 43–59 (2025).

[16] Han, L., Wang, D. & Li, F. Multi-scale dual-path attention network for seismic background noise attenuation. *Scientific Reports* **15**, 41525 (2025). URL https://www.nature.com/articles/s41598-025-25446-x.

[17] Yao, Z., Hao, L., Qin, L., Chen, J. & Li, W. Efficient seismic data denoising via multi-scale attention network with depthwise separable and residual dilated convolutions. *Scientific Reports* **16**, 2818 (2026). URL https://www.nature.com/articles/s41598-025-32591-w.

[18] Peng, J., Li, Y., Liao, Z., Wang, X. & Yang, X. Seismic data strong noise attenuation based on diffusion model and principal component analysis. *IEEE Transactions on Geoscience and Remote Sensing* **62** (2024).

[19] Chen, H., Wang, J. & Liu, B. Dual-domain mamba for seismic random noise suppression. *Journal of Applied Geophysics* **243** (2025).

[20] Zhang, M., Jing, C., Cui, Y., Liu, Y. & Chen, G. Unsupervised seismic random noise attenuation via 3d enhanced multiscale features. *Geophysics* **90**, V587–V599 (2025).

[21] Wang, S., Luo, Y., Li, S., Peng, J. & Wu, B. Efficient seismic random noise attenuation via KAN-empowered neural low-rank representation. *IEEE Transactions on Geoscience and Remote Sensing* **63** (2025).

[22] Sun, H., Yang, F. & Ma, J. Seismic random noise attenuation via self-supervised transfer learning. *IEEE Geoscience and Remote Sensing Letters* **19**, 1–5 (2022).

[23] Chen, W. *et al.* Unsupervised noise suppression method for depth network seismic data based on prior information constraint. *Coal Geology and Exploration* **49**, 249–256 (2021).

[24] Wu, X. *et al.* Building realistic structure models to train convolutional neural networks for seismic structural interpretation. *Geophysics* **85**, WA27–WA39 (2020).

[25] Sheng, H. *et al.* Seismic foundation model: A next generation deep-learning model in geophysics. *Geophysics* **90**, IM59–IM79 (2025).

[26] Zhao, T., Ouyang, L. & Chen, T. Seismic random noise attenuation via low-rank tensor network. *Applied Sciences-Basel* **15** (2025).

[27] Xiao, L. The fusion of data-driven machine learning with mechanism models and interpretability issues. *Geophysical Prospecting for Petroleum* **61**, 205–212 (2022).

[28] Liu, Q. & Ma, J. Generative interpolation via a diffusion probabilistic model. *Geophysics* **89**, V65–V85 (2024).

[29] Liu, B. *et al.* Unsupervised deep learning for random noise attenuation of seismic data. *IEEE Geoscience and Remote Sensing Letters* **19** (2022).

[30] Jun, H. & Kim, H.-J. Loss functions in machine learning for seismic random noise attenuation. *Geophysical Prospecting* **72**, 978–995 (2024).

[31] Yang, L. *et al.* Interpretable unsupervised learning framework for multidimensional erratic and random noise attenuation. *IEEE Transactions on Geoscience and Remote Sensing* **62**, 1–20 (2024).

[32] Zhao, M., Zhong, S., Fu, X., Tang, B. & Pecht, M. Deep Residual Shrinkage Networks for Fault Diagnosis. *IEEE Transactions on Industrial Informatics* **16**, 4681–4690 (2020).

[33] Zhao, Q., Du, Q., Gong, X. & Chen, Y. Signal-Preserving Erratic Noise Attenuation via Iterative Robust Sparsity-Promoting Filter. *IEEE Transactions on Geoscience and Remote Sensing* **56**, 3547–3560 (2018).

[34] Cui, Y., Bin Waheed, U. & Chen, Y. Unsupervised deep learning for DAS-VSP denoising using attention-based deep image prior. *IEEE Transactions on Geoscience and Remote Sensing* **63**, 1–14 (2025).

[35] Cui, Y., Bai, M., Wu, J. & Chen, Y. Earthquake signal detection using a multiscale feature fusion network with hybrid attention mechanism. *Geophysical Journal International* **240**, 988–1008 (2024).

[36] Yang, L., Chen, Y., Siervo, D., Vallejo, K. & Savvaidis, A. QBTransNet: deep learning earthquake distinction from quarry blasts using dilated convolutional transformer. *Seismological Research Letters* **96**, 3207–3220 (2025).

[37] Chen, W., Chen, M., Guo, R. & Yang, L. Seismic data enhancement method based on residual shrinkage network. *Journal of Yangtze University (Natural Science Edition)* **22**, 1–11 (2025).

[38] Saad, O. M. *et al.* Self-Attention Deep Image Prior Network for Unsupervised 3-D Seismic Data Enhancement. *IEEE Transactions on Geoscience and Remote Sensing* **60**, 1–14 (2022).

[39] Chen, M. *Study on Seismic Data Enhancement Method Based on Residual Shrinkage Network*. Master's thesis, Yangtze University (2025).

[40] Zheng, X. *et al.* The transformer architecture-based glt-unet network for seismic data denoising. *Geophysical Prospecting for Petroleum* **65**, 427–441 (2026).

[41] Zhang, Z., Li, C., Zhao, H., Wang, J. & Zhu, S. 3-d seismic denoising via a dual-guided diffusion model driven by fourier neural operators. *Geoenergy Science and Engineering* **262** (2026).

[42] Chen, G., Liu, Y. & Zhang. Vectorized seismic random noise attenuation based on an unsupervised monte carlo deep learning framework. *Chinese Journal of Geophysics (in Chinese)* **69**, 366–382 (2026).

[43] Shekhar, N. & Elumalai, K. DEAE-INR: dual encoder based autoencoders with implicit neural representations for seismic random noise attenuation. *IEEE Journal of Selected Topics in Applied Earth Observations and Remote Sensing* **19**, 14401–14418 (2026).